

Ferroelectricity Induced by Ordering of Twisting Motion in a Molecular Rotor

Yi Zhang,[†] Wen Zhang,^{*,†} Shen-Hui Li,^{*,‡} Qiong Ye,[†] Hong-Ling Cai,[†] Feng Deng,^{*,‡} Ren-Gen Xiong,^{*,†} and Songping D. Huang[§]

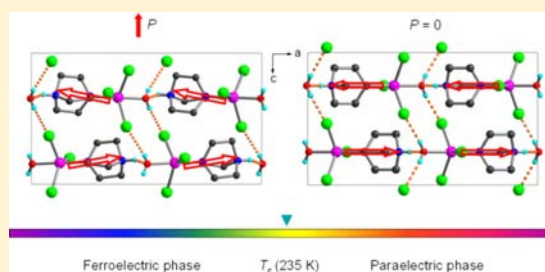
[†]Ordered Matter Science Research Center, Southeast University, Nanjing 211189, P. R. China

[‡]State Key Laboratory Magnetic Resonance and Atomic Molecular Physics, Wuhan Center for Magnetic Resonance, Wuhan Institute of Physics and Mathematics, Chinese Academy of Sciences, Wuhan 430071, P. R. China

[§]Department of Chemistry, Kent State University, Kent, Ohio 44240, United States

Supporting Information

ABSTRACT: A novel mononuclear metal–organic compound, [Cu(Hdabco)(H₂O)Cl₃] (**1**, dabco = 1,4-diazabicyclo[2.2.2]octane) in which the Cu^{II} cation adopts a slightly distorted bipyramidal geometry where the three Cl anions constitute the equatorial plane and the Hdabco cation and H₂O molecule occupy the two axial positions, was synthesized. Its paraelectric-to-ferroelectric phase transition at 235 K (T_c) and dynamic behaviors were characterized by single crystal X-ray diffraction analysis, thermal analysis, dielectric and ferroelectric measurements, second harmonic generation experiments, and solid-state nuclear magnetic resonance measurements. Compound **1** behaves as a molecular rotor above room temperature in which the (Hdabco) part rotates around the N...N axis as a rotator and the [Cu(H₂O)Cl₃] part acts as a stator. In the temperature range 235–301 K, a twisting motion of the rotator is confirmed. Below the T_c , the motions of the rotor are frozen and the molecules become ordered, corresponding to a ferroelectric phase. Origin of the ferroelectricity was ascribed to relative movements of the anions and cations from the equilibrium position, which is induced by the order–disorder transformation of the twisting motion of the molecule between the ferroelectric and paraelectric phases. Study of the deuterated analogue [Cu(Ddabco)(D₂O)Cl₃] (**2**) excludes the possibility of proton ordering as the origin of the ferroelectricity in **1**.



INTRODUCTION

Ferroelectric materials, as a special kind of polar materials, have long drawn great interest due to their rich physical-chemical properties for fundamental research and various industrial applications.¹ One of the biggest challenges in ferroelectric materials is always the rational design of novel systems. Solutions to this problem rely on a deep understanding of structure–function relationship in ferroelectrics which will further promote emergence of high-performance polar materials. Organic–inorganic hybrid ferroelectrics offer more opportunities and potentials on this aspect than conventional pure inorganic oxide ferroelectrics due to diverse choices and organizations of the organic and inorganic components or building blocks. Origin of ferroelectricity in these hybrid systems can be roughly ascribed to the cooperative motions of atoms or polar components in the crystal lattices, such as reorientations of dipolar molecules and displacements of ions (e.g., dynamic protons in hydrogen bonds).²

Recently, molecular rotors afford a new way to construct novel molecular ferroelectrics due to the rotations of the polar rotators in the crystal lattices if well designed and assembled. At a first glance, it seems a common sense that a “flexible” molecular rotation is required for dipole reorientations to

trigger ferroelectric orderings, that is, a low enough energy barrier for the reorientations. However, this free rotation hardly leads to ferroelectricity if no cooperativity occurs among the dipoles. On the other hand, closely packed polar molecules give little room to rotate to rearrange the dipoles within them. Therefore, a delicate balance should be taken into consideration between free rotation and freezing for designing this type of molecular ferroelectrics. A hint is the realization of a molecular ferroelectric may be possible based on twisting of constrained molecular rotors.³ From the molecular designing point of view, 1,4-diazabicyclo[2.2.2]octane (dabco), a highly symmetric tertiary diamine with a globular shape, can act as a rotator part of molecular rotors.⁴

The first appearance of dabco in ferroelectric compounds was reported by Katrusiak and Szafranski who successfully constructed hydrogen-bonded organic salts, [Hdabco]X (X = ClO₄, BF₄, and ReO₄).⁵ In this series of ferroelectric compounds, the monovalent [Hdabco]⁺ cations are head-to-tail linked linearly by N–H...N bonds in which the protons can undergo reversibly bistable orientations by a collective proton-

Received: May 16, 2012

Published: June 11, 2012

transfer process. In our recent studies, the $[\text{H}_2\text{dabco}]^{2+}$ cations were utilized in metal–organic hybrid ferroelectrics in which the order–disorder transitions of the dications arouse the corresponding paraelectric-to-ferroelectric phase transitions.⁶ These studies reveal that the dabco component has the potential to undertake a key role in designing and constructing new ferroelectrics due to its striking features as donor–acceptor of proton or order–disorder transformation.

As a continuation of our research of organic–inorganic hybrid ferroelectrics,⁷ we hereby report a new rotor-like mononuclear metal–organic ferroelectric compound $[\text{Cu}(\text{Hdabco})(\text{H}_2\text{O})\text{Cl}_3]$ (**1**) showing a distinct ferroelectric phase transition at 235 K. Ordering of twisting motion of the molecule constrained in a hydrogen bond network is found to induce the ferroelectric phase. To our best knowledge, the ferroelectric metal complex with coordinated dabco ligand is unprecedented even through there is intensive research focused on dabco as cations.⁸

EXPERIMENTAL SECTION

Synthesis. All reagents and solvents in the syntheses were of reagent grade and used without further purification. Green crystals of **1** were grown from an aqueous solution containing $[\text{Hdabco}]\text{Cl}$ and CuCl_2 with a yield of 24%. The deuterated analog $[\text{Cu}(\text{Ddabco})(\text{D}_2\text{O})\text{Cl}_3]$ (**2**) was prepared from a D_2O solution. The phase purity is confirmed by its IR and XRD matching with its single crystal structural determination (see Supporting Information).

Measurement Methods. Infrared (IR) spectra were recorded on a Shimadzu IRPrestige-21. Powder X-ray diffraction (PXRD) was measured on a Rigaku D/MAX 2000 PC X-ray diffraction instrument. DSC measurements were performed on a PerkinElmer Diamond DSC under nitrogen atmosphere in aluminum crucibles with a heating or cooling rate of 10 K/min. Specific heat analyses were carried out on a Quantum Design PPMS. For dielectric measurements, the samples were made with the powder sample-pressed pellets. Silver conduction paste deposited on the surfaces was used as the electrodes. Complex dielectric permittivities were measured with an Agilent or a TH2828A impedance analyzer over the frequency range from 1 kHz to 1 MHz with an applied electric field of 0.5 V. For second harmonic generation (SHG) experiments, an unexpanded laser beam with low divergence (pulsed Nd:YAG at a wavelength of 1064 nm, 5 ns pulse duration, 1.6 MW peak power, 10 Hz repetition rate) was used. The instrument model is FLS 920, Edinburgh Instruments and the low temperature system is 10–325 K, DE 202, while the laser is Vibrant 355 II, OPOTEK. The numerical values of the nonlinear optical coefficients for SHG have been determined by comparison with a KDP reference. All variable temperature (VT) solid-state nuclear magnetic resonance (SSNMR) experiments were carried out on a Varian Infinityplus-300 spectrometer with a 4 mm double-resonance MAS probe at resonance frequencies of 299.8, 46.0, and 75.4 MHz for ^1H , ^2H , and ^{13}C , respectively. ^{13}C MAS NMR spectra were acquired with direct polarization. The sample was spun at 12 kHz and the pulse delay was set to 0.03 s. Typically 10 000–70 000 scans were accumulated for the ^{13}C MAS NMR measurement. ^1H single pulse NMR spectra was recorded with a pulse length of 4 μs , a recycle delay of 0.03 s, and a spinning rate of 12 kHz. Static ^2H NMR spectra was obtained by using quadrupole echo. The sample temperatures were calibrated by the chemical shifts of $\text{Pb}(\text{NO}_3)_2$ under the same condition in the variable temperature (VT) NMR experiments.

Single-Crystal X-ray Crystallography. X-ray diffraction experiments were carried out using a Rigaku Saturn 924 diffractometer with $\text{Mo K}\alpha$ radiation ($\lambda = 0.71073 \text{ \AA}$) at various temperatures. Data collection, cell refinement, and data reduction were performed by using the CrystalClear software package (Rigaku). The structures of **1** and **2** were solved by direct methods and refined by the full-matrix method based on F2 using the SHELXLTL software package. All non-hydrogen atoms were refined anisotropically, and the positions of all

hydrogen atoms were generated geometrically. Crystal data for **1** at 298 K: $\text{C}_6\text{H}_{15}\text{Cl}_3\text{CuN}_2\text{O}$, $M_w = 301.09$, orthorhombic $Pnma$, $a = 15.729(3) \text{ \AA}$, $b = 9.041(2) \text{ \AA}$, $c = 7.795(2) \text{ \AA}$, $V = 1108.6(4) \text{ \AA}^3$, $Z = 4$, $D_c = 1.804 \text{ Mg m}^{-3}$, $R_1 (I > 2\sigma) = 0.0315$, $wR_2 = 0.0769$, $\mu = 2.657 \text{ mm}^{-1}$, $S = 1.125$; **1** at 173 K: orthorhombic $Pna2_1$, $a = 15.830(8) \text{ \AA}$, $b = 7.718(4) \text{ \AA}$, $c = 9.003(4) \text{ \AA}$, $V = 1099.9(9) \text{ \AA}^3$, $Z = 4$, $D_c = 1.818 \text{ Mg m}^{-3}$, $R_1 (I > 2\sigma) = 0.0181$, $wR_2 = 0.0533$, $\mu = 2.678 \text{ mm}^{-1}$, $S = 1.097$, Flack value = 0.45(2). Crystal data for **2** at 298 K: $\text{C}_6\text{H}_{12}\text{Cl}_3\text{CuD}_3\text{N}_2\text{O}$, $M_w = 304.11$, orthorhombic $Pnma$, $a = 15.818(3) \text{ \AA}$, $b = 9.0950(18) \text{ \AA}$, $c = 7.8500(16) \text{ \AA}$, $V = 1129.4(4) \text{ \AA}^3$, $Z = 4$, $D_c = 1.789 \text{ Mg m}^{-3}$, $R_1 (I > 2\sigma) = 0.0275$, $wR_2 = 0.0677$, $\mu = 2.608 \text{ mm}^{-1}$, $S = 1.056$; **2** at 173 K: orthorhombic $Pna2_1$, $a = 15.847(7) \text{ \AA}$, $b = 7.682(3) \text{ \AA}$, $c = 8.976(4) \text{ \AA}$, $V = 1092.7(8) \text{ \AA}^3$, $Z = 4$, $D_c = 1.849 \text{ Mg m}^{-3}$, $R_1 (I > 2\sigma) = 0.0197$, $wR_2 = 0.0497$, $\mu = 2.696 \text{ mm}^{-1}$, $S = 1.053$, Flack value = 0.506(10).

RESULTS AND DISCUSSION

Crystal Structures of 1. Variable-temperature X-ray structure determinations of **1** were performed at 293 K (high-temperature phase, HTP) and 173 K (low-temperature phase, LTP), respectively. At 293 K, **1** crystallizes in the orthorhombic crystal system $Pnam$ (No. 62; nonstandard setting).⁹ The basic structural unit is mononuclear $[\text{Cu}(\text{Hdabco})(\text{H}_2\text{O})\text{Cl}_3]$, like a three-tail bacteriophage (Figure 1a). The Cu^{II} ion adopts a distorted trigonal-bipyramidal

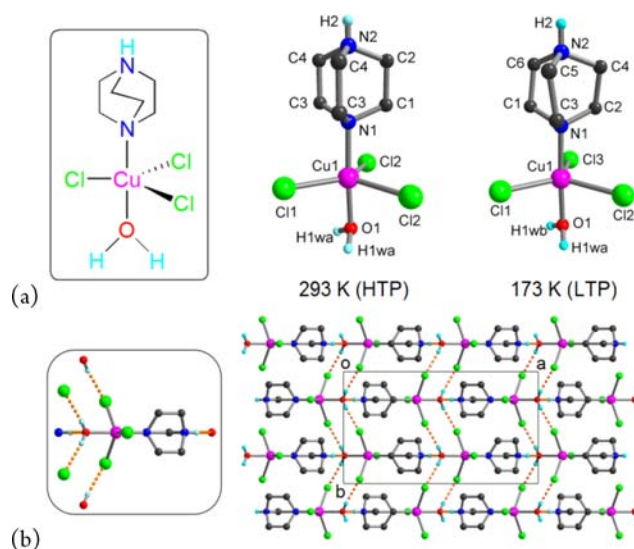


Figure 1. (a) Molecular structures of **1** at room temperature. Hydrogen atoms on carbon atoms are omitted for clarity. (b) Hydrogen-bonding structure of **1** (293 K) viewed along the c axis.

geometry in which the two apical atoms are one N atom from $[\text{Hdabco}]^+$ cation and one O atom from H_2O , respectively, and three equatorial atoms are Cl anions. It is notable that the bond lengths of the three Cu–Cl bonds are strikingly different, that is, one is 2.285(1) \AA (Cu1–Cl1) and the other two 2.4189(7) \AA (Cu1–Cl2).

There are full of hydrogen bonds of $\text{N–H}\cdots\text{O}$ and $\text{O–H}\cdots\text{Cl}$ among the $[\text{Cu}(\text{Hdabco})(\text{H}_2\text{O})\text{Cl}_3]$ units (Figure 1b and Supporting Information). Along the a axis, the units are head-to-tail connected via $\text{N–H}\cdots\text{O}$ hydrogen bonds, forming zigzag chains. Furthermore, the chains are connected through rich $\text{O–H}\cdots\text{Cl}$ hydrogen bonds among the water molecules and Cl anions. As to the $[\text{Cu}(\text{Hdabco})(\text{H}_2\text{O})\text{Cl}_3]$ unit, the $[\text{Cu}(\text{H}_2\text{O})\text{Cl}_3]$ part seems held tightly in the three-dimensional hydrogen bonding network.

At 173 K, **1** crystallizes in space group $Pna2_1$, indicating a structural phase transition. In the structural unit, the Cu^{II} ions still adopts the distorted trigonal-bipyramidal geometry (Figure 1a). However, the bond lengths of the three $\text{Cu}-\text{Cl}$ bonds are all different: $\text{Cu1}-\text{Cl1} = 2.294(1)$ Å, $\text{Cu1}-\text{Cl2} = 2.408(2)$ Å, and $\text{Cu1}-\text{Cl3} = 2.437(1)$ Å. Meanwhile, conformations of the rings of the dabco ligand show a little difference at the both temperature phases. The average values of the $\text{N}-\text{C}-\text{C}-\text{N}$ torsion angles are 0° in the HTP and 17° in the LTP, respectively.

From the viewpoint of symmetry breaking, the HTP crystallizes in the centrosymmetric point group mmm and the LTP in a polar point group $mm2$, well consistent with a paraelectric-to-ferroelectric phase transition with an Aizu notation $mmmFmm2$ (Figure 2). The loss of the mirror

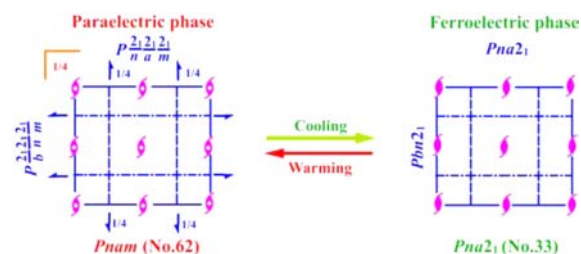


Figure 2. A change of symmetry elements of **1** from 8 (E , C_2 , $2C'_2$, i , σ_h , $2\sigma_v$) in the HTP (paraelectric phase) to 4 (E , C_2 , $2\sigma_v$) in the LTP (ferroelectric phase).

symmetric element (m) is aroused by slight displacements of the atoms in **1** in the LTP, though these changes are very small and exert nearly negligible influence on the cell parameters.

Paraelectric-to-Ferroelectric Phase Transition of **1**.

Phase transition temperature (T_c) of **1** is determined by thermal analyses including differential scanning calorimetry (DSC) and specific heat capacity (SHC). DSC measurement shows a pair of peaks on cooling and heating centered around 235 K as shown in Figure 3. Estimated entropy change of the phase transition is ca. $0.4 \text{ kJ}\cdot\text{mol}^{-1}$ by the SHC measurement, suggesting that this phase transition may be of second order.

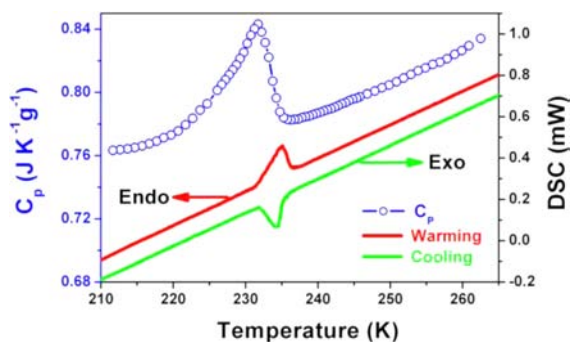


Figure 3. Curves of specific heat capacity and differential scanning calorimetry of **1** as a function of temperature.

Variable-temperature dielectric constant measurement of **1** shows an anomaly at about 234 K on cooling and 237 K on warming (Figure 4). The peak value reaches 24 along the c axis, while in the other directions, the curves only show nearly negligible anomalies with values averaged at about 4.5 in the measured temperature range. A fit to the Curie–Weiss law, $\epsilon = C/(T - T_0)$ where ϵ is the dielectric constant, C is the Curie

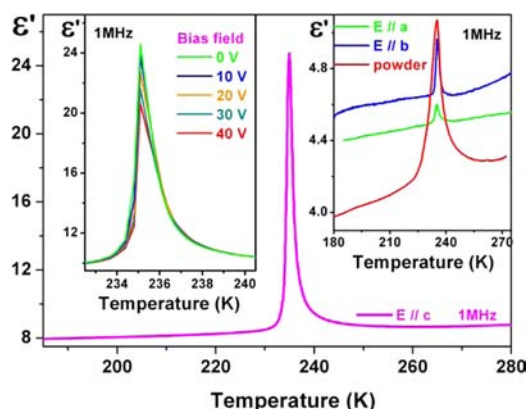


Figure 4. Variable-temperature dielectric constant of **1** along the three axes in cooling mode. Inset: (left) the temperature-dependence of dielectric constant under biased electric field along the c axis; (right) the temperature-dependence of dielectric constant along the a and b axis and on powdered sample. The measured frequency is fixed at 1 MHz.

constant, T is the temperature, and T_0 is the Curie–Weiss temperature, affords a ratio of the C in the paraelectric phase to the ferroelectric phase $C_{\text{para}}/C_{\text{ferro}} = 2.0$, indicating that the phase transition is of second order. The dielectric constant measured at different frequencies (50 Hz to 1 MHz) shows a frequency-independent property, suggesting nonoccurrence of a relaxation process in the low frequency range. In addition, there is no large change of dielectric constant under applied electric field, indicating that **1** is not an electrically tunable dielectric.

The genuine characteristics of ferroelectricity of **1** were demonstrated by the measurements of dielectric hysteresis loops and variable-temperature second harmonic generation (SHG). Dielectric hysteresis loops of **1** were recorded with a Sawyer–Tower circuit at 10–33 Hz (Figure 5). Upon cooling,

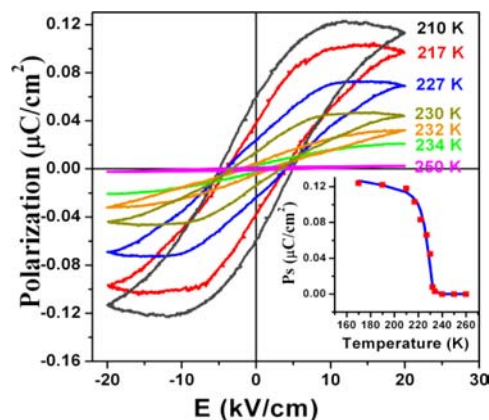


Figure 5. Dielectric hysteresis loops of **1** recorded at 10–33 Hz. Inset: the temperature-dependence of saturated polarization P_s .

the loop appears just below the T_c . The saturated polarization P_s increases quickly and reaches its maximum value of about $0.12 \mu\text{C}\cdot\text{cm}^{-2}$ below 210 K. The corresponding coercive field is about $5 \text{ kV}\cdot\text{cm}^{-1}$. The relatively small P_s may be related to its structural origin.

The temperature-dependent SHG signal emerges below the T_c (Figure 6). It unambiguously indicates a structural change from a centrosymmetric to a noncentrosymmetric one as

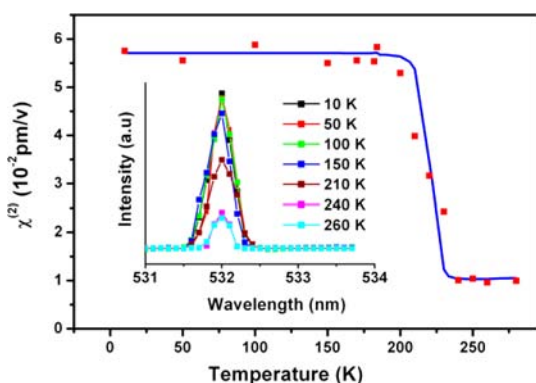


Figure 6. Temperature-dependence of second harmonic generation of **1**. Inset: the photoluminescence strength at 532 nm.

shown in X-ray diffraction analyses discussed above. The value of the temperature-dependent effective second-order nonlinear optic susceptibility $\chi^{(2)}$ changes in the same trend as the P_s on cooling, and is well consistent with the Landau relationship $\chi^{(2)} = 6\epsilon_0\beta P_s$, where β is almost independent of the temperature. Both the variations of the P_s and $\chi^{(2)}$ in the vicinity of the T_c are continuous, revealing a second-order phase transition.^{2c}

Dynamic Behaviors of 1. To have a deeper insight into the phase transition, we tried to perform VT-SSNMR experiments on **1**.

In the ^{13}C MAS NMR spectra of **1** at different temperatures (Figure 7), three signals are observable: the signals at around

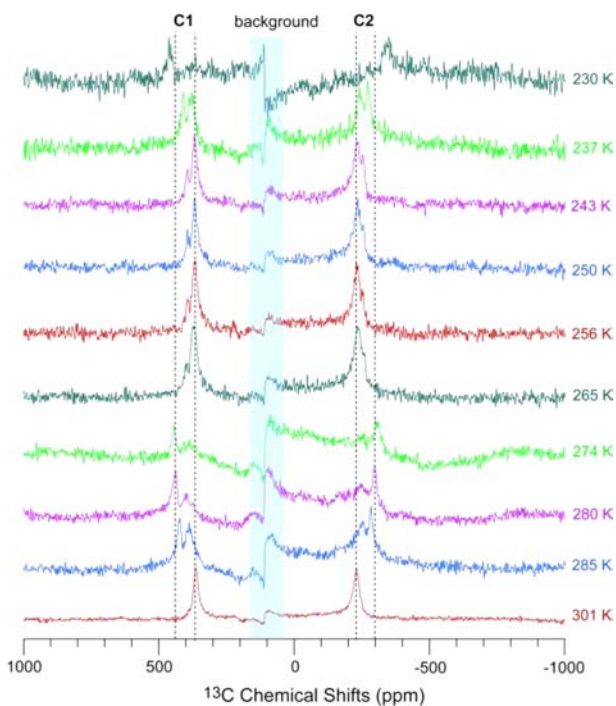


Figure 7. ^{13}C MAS NMR spectra of **1** acquired at different temperatures.

320–480 ppm are tentatively assigned to the C1 site (C1 and C3 atoms in the HTP) in the ethylene bridges; the signals at around -360 to -220 ppm are ascribed to the C2 site (C2 and C4 atoms in the HTP) in the ethylene bridges; the distorted peak at around 109 ppm is due to the background signal from NMR rotor. The ^{13}C chemical shifts of ethylene bridges

obviously deviate from the normal ^{13}C chemical shift region (around 30 ppm), which may result from the Cu^{2+} paramagnetic effect in the sample. The paramagnetic effect can induce both chemical shift and relaxation time variations which are strongly dependent on the distances between the paramagnetic ion and the observed nuclei.

The CH_2 signals in **1** can be well resolved at a MAS speed of 12 kHz without heteronuclear decoupling and no significant improvement can be achieved as the decoupling is applied. In comparison, the CH_2 group signals in rigid systems (such as amino acids) cannot be detected at 12 kHz without heteronuclear decoupling, suggesting that the ethylene bridges in **1** undergo fast rotational motion around the 3-fold $\text{N}\cdots\text{N}$ axis above 237 K.

The ^{13}C NMR chemical shifts of ethylene bridges are sensitive to temperature. In the temperatures range from 237 to 285 K, two sets of ^{13}C NMR signals from the ethylene bridges are observable in most of ^{13}C NMR spectra, which is probably due to the different orientations of ethylene bridges in **1**. The reorientation of ethylene bridges comes from its small angle twisting motion. When the temperature is lowered below 230 K, the rotational motion of ethylene bridges is likely significantly restricted and the paramagnetic effect becomes pronounced, which makes it difficult to acquire the ^{13}C NMR spectra.

The ^1H NMR spectra of **1** remain almost unchanged from 301 to 243 K (Figure 8). The signals become broadened at 230

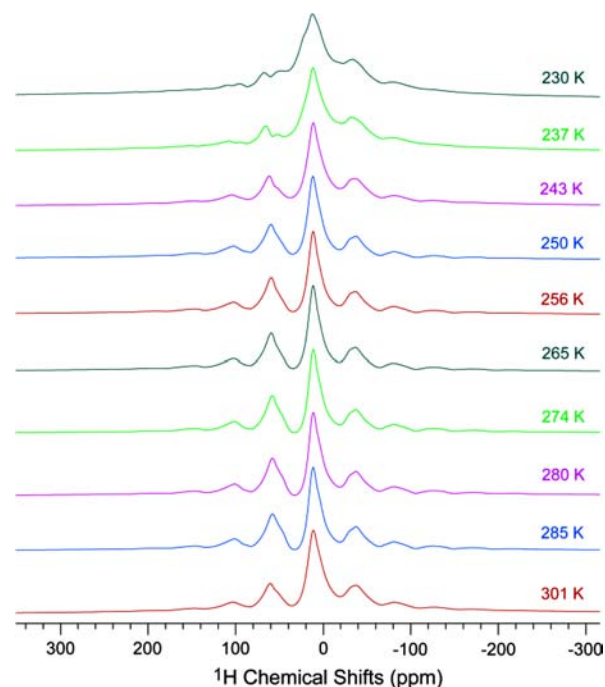


Figure 8. ^1H NMR spectra of **1** acquired at different temperatures.

K compared to 243 K, indicating that fast rotational motion in **1** was mostly frozen at that temperature. After careful deconvolution of the ^1H NMR spectra of **1** (see Supporting Information), two major peaks and their spinning sidebands could be clearly observed. The signals at 12.6 and 5.1 ppm are assigned to the ethylene bridges and coordinated water, respectively. As temperature decreased to 230 K, the chemical shifts of the main peak (12.6 ppm) remain unchanged, while its line width becomes broader, which could probably due to the

rigidity of sample **1** at the low temperature. In addition, the appearance of a small peak at around 26.0 ppm can be attributed to the NH group having strong hydrogen bond with H₂O. As water is frozen at that temperature, the hydrogen bond between H₂O and NH group should be strengthened, resulting in the chemical shift movement of NH group to downfield.

The ²H NMR spectra of **2** are acquired at variable temperatures (see Supporting Information). The resonance at around -1900 ppm is assigned to the D₂O directly coordinated to the Cu^{II} ion (see Supporting Information). The Pake pattern signal is due to the ND group. The quadrupolar splitting of ND group in **2** is determined to be ranged from 67 to 77 kHz. In comparison with that of 125 kHz in rigid systems, the order parameter of the ND group could be estimated to be around 0.54–0.62, confirming the rotational molecular motion of ethylene bridges at the temperatures. It is also shown that the molecular motions of both D₂O and ND in **2** are not sensitive to the temperature.

The disorder characteristics of the dabco ring in the HTP are also evidenced by the crystal structural analysis at room temperature. One proof is the thermal ellipsoids of the end C atoms are relatively large, indicating averaged effect of the disordered atoms. It is also seen that the ethylene groups in the ring of dabco adopt totally eclipsed conformation which is not the actual state but an averaged result of two slightly staggered conformations as seen in the low-temperature phase of **1**. It means the Hdabco cation exhibits disorder in the HTP. In the LTP, the Hdabco cation is ordered, showing deviation from an ideal *D*_{3h} symmetry, with the highest absolute value of the C–N–N–C torsion angle among the major positions of 5°. It adopts a slightly twisted conformation with torsion angles of N1–C1–C6–N2 = 16 and N1–C2–C4–N2 = 18.

Density functional theory (DFT) calculations were carried out on **1** in order to investigate the rotational possibility of the dabco molecule and Cu–Cl coordination environment. The hybrid functional B3LYP with the LANL2DZ basis set for the Cu atom and 6-31G(d) basis set for C, N, O, Cl, and H atoms was employed. The nearest-neighboring molecules around the dabco or Cu–Cl coordination environment have been involved in the calculation mode, so the calculation mode contains five [Cu(Hdabco)Cl₃(H₂O)] molecules, that is, one molecule is surrounded by the other four ones (see Supporting Information).

The atomic coordinates of **1** based on the X-ray crystal structural analysis in the LTP were used for the calculations. The initial atomic coordinates from the X-ray crystal structural analysis corresponded to the first potential energy minimum at $\varphi = 0$. The relative energy of the structures was obtained by evaluating the rigid rotation of dabco by fixing the Cu center and along the Cu–N coordination bonds. The relative energies were calculated using fixed atomic coordinates at every 30°. For rotational angle φ of the dabco molecule, three potential minimum at $\varphi = 0^\circ$, $\varphi = 120^\circ$, and $\varphi = 240^\circ$ have been observed (Figure 9a). The triple minimum potential energy curve suggested a probability of a 120° hopping of the dabco. Potential energy barriers of ca. 140, 100, and 110 kJ mol⁻¹ were observed at $\varphi = 60^\circ$, $\varphi = 180^\circ$, and $\varphi = 300^\circ$, respectively.

For the Cu–Cl coordination environment, its 360° rotation along the O–Cu–N axis is very difficult to realize owing to the steric hindrance from neighboring molecules. Possibility of a small-angle rotation of the Cu–Cl coordination environment along the Cu–N bond in the range of -30 to +30° has been investigated every 5° (Figure 9b). The calculation results

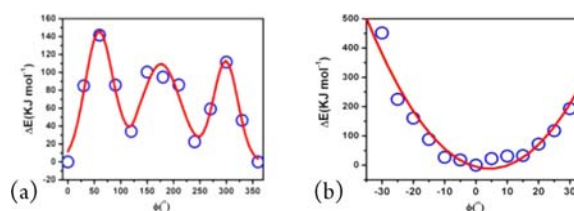


Figure 9. (a) Potential energy curves for rotational angle φ of a 360° rotation of the dabco molecule; (b) -30 to +30° twisting motion of Cu–Cl coordination environment along the Cu–N bond.

indicate this motion is still not so easy to realize owing to very high energy barriers. However, it is still possible that the Cu–Cl coordination environment takes a motion in the range of about -10° to +10° along the O–Cu–N axis.

Origin of Ferroelectricity of **1.** From above studies, it becomes clear that the [Cu(Hdabco)(H₂O)Cl₃] is a molecular rotor and undergoes motion changes with the decrease of temperature. Above room temperature, the molecule behaves as an active rotor in which the (Hdabco) part rapidly rotates around the N···N axis as a rotator and the [Cu(H₂O)Cl₃] part, tightly held by a strong intermolecular hydrogen bond network, acts as a stator (not strictly static). In the temperature range 235–301 K, a twisting motion of the rotator is confirmed. Below the *T_c*, the motions of the rotor are frozen and the molecules become ordered, corresponding to a ferroelectric phase.

The source of power for the twisting motion is thought to come from thermal vibrations of the dabco ligand around the equilibrium position. In the HTP, it is seen that the dabco rings exhibits disorder, corresponding to a disordered state or paraelectric phase. As temperature decreases below the *T_c*, energy barrier centered around the equilibrium position becomes large enough to preclude thermally disordering of the twisting motion. Two energetically equal sites, separated by the equilibrium position, can be distinguished and related by a 5° rotation around the N···N axis. The molecule occupies one of the two sites due to an insurmountable energy barrier, corresponding to an ordered state or ferroelectric phase. A transition between the two sites is thermally prohibited but allowed under an alternating electrical field. This description follows a symmetric double-well potential model which needs a further investigation for more detailed information.

The twisting motion of the dabco ligand in the molecule triggers movements of ions from their equilibrium positions, especially the [Cu(H₂O)Cl₃] part, to result in polarization or ferroelectricity in **1** (Figure 10). Therefore, the polarization of **1** may be calculated from the relative displacements of the three Cl anions, the Cu^{II} center ion, and the proton on the N atom from their equilibrium positions within the unit cell. Following this assertion, the *P_s* is estimated to be 0.28 μC·cm⁻² at 173 K based on point electric charge calculation in which the Cl2 ion has the biggest contribution (see Supporting Information). This value is fairly consistent with the measured value of 0.12 μC·cm⁻² at 210 K.

The role of the coordinated water molecule should not be underemphasized. First, it assembles every mononuclear molecule into a hydrogen-bonded network. The [Cu(H₂O)Cl₃] part is well anchored in the crystal lattice via hydrogen bonds, enabling it as a stator of the molecular rotor while the only one hydrogen bond at the head of the Hdabco leaves much room for its free rotation as a rotator. More importantly, the

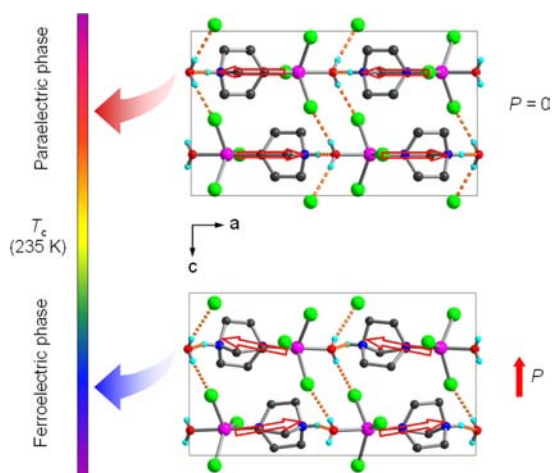


Figure 10. Schematic diagram of the appearance of the spontaneous polarization (P) of **1** during the paraelectric-to-ferroelectric phase transition. Hollow red arrows denote permanent dipole moments of the molecules and hydrogen atoms on carbon atoms are omitted for clarity.

hydrogen bond network exerts delicate constraints on the motions of the molecule in the LTP to result in cooperative intermolecular interactions. This is indispensable for the occurrence of ferroelectricity in crystalline samples which is essentially a result of long-range coupling interactions.

Since there is a type of hydrogen-bond ferroelectrics in which specific motions of the proton lead to paraelectric-to-ferroelectric phase transition,⁵ the deuterated analog **2** was synthesized. It is notable that **2** shows the same dielectric behaviors as **1** without any obvious isotope effects, clearly excluding the role of proton dynamics in the paraelectric-to-ferroelectric phase transition of **1**.

CONCLUSION

This work has successfully demonstrated that the monocoordinated dabco–Cu complex $[\text{Cu}(\text{Hdabco})(\text{H}_2\text{O})\text{Cl}_3]$ (**1**) displays paraelectric-to-ferroelectric phase transition at 235 K (T_c). Above room temperature, **1** behaves as an active rotor in which the (Hdabco) part rapidly rotates around the N...N axis as a rotator and the $[\text{Cu}(\text{H}_2\text{O})\text{Cl}_3]$ part acts as a stator. In the temperature range 235–301 K, a twisting motion of the rotator is confirmed. Below the T_c , the motions of the rotor are frozen and the molecules become ordered, corresponding to a ferroelectric phase. Origin of the ferroelectricity was ascribed to the movements of the anions and cations from the equilibrium position, which is induced by the order–disorder transformation of the twisting motion of the dabco ligand between the ferroelectric and paraelectric phases. This example is a model compound to disclose connections between molecular rotors and molecular ferroelectrics. It points out a new way to design novel multifunctional molecular devices.

ASSOCIATED CONTENT

Supporting Information

Experimental section, Figures S1–S11, Tables S1–S3, and CIF files. This material is available free of charge via the Internet at <http://pubs.acs.org>.

AUTHOR INFORMATION

Corresponding Author

zhangwen@seu.edu.cn; lishenhui@wipm.ac.cn; dengf@wipm.ac.cn; xiongrg@seu.edu.cn

Notes

The authors declare no competing financial interest.

ACKNOWLEDGMENTS

This work was supported by the NSFC (grants 20931002, 90922005, 21071030, 21101025, 21003154 and 20921004) and NSF of Jiangsu Province (grants BK2008029, BK2010425).

REFERENCES

- (1) (a) Jona, F.; Shirane, G. *Ferroelectric Crystals*; Pergamon Press: New York, 1962. (b) Mitsui, T.; Tatsuzaki, I.; Nakamura, E. *An Introduction to the Physics of Ferroelectrics*; Gordon and Breach Science Publishers: New York, 1976. (c) Lines, M. E.; Glass, A. M. *Principles and Application of Ferroelectrics and Related Materials*; Oxford University Press: Oxford, 2001.
- (2) (a) Horiuchi, S.; Tokura, Y. *Nat. Mater.* **2008**, *7*, 357. (b) Hang, T.; Zhang, W.; Ye, H.-Y.; Xiong, R.-G. *Chem. Soc. Rev.* **2011**, *40*, 3577. (c) Zhang, W.; Xiong, R.-G. *Chem. Rev.* **2012**, *112*, 1163.
- (3) Akutagawa, T.; Koshinaka, H.; Sato, D.; Takeda, S.; Noro, S.; Takahashi, H.; Kumai, R.; Tokura, Y.; Nakamura, T. *Nat. Mater.* **2009**, *8*, 342.
- (4) (a) Jarowski, P. D.; Houk, K. N.; Garcia-Garibay, M. A. *J. Am. Chem. Soc.* **2007**, *129*, 3110. (b) Gould, S. L.; Tranchemontagne, D.; Yaghi, O. M.; Garcia-Garibay, M. A. *J. Am. Chem. Soc.* **2008**, *130*, 3246. (c) Karlen, S. D.; Reyes, H.; Taylor, R. E.; Khan, S. I.; Hawthorne, M. F.; Garcia-Garibay, M. A. *Proc. Natl. Acad. Sci. U.S.A.* **2010**, *107*, 14973. (d) Lemouchi, C.; Vogelsberg, C. S.; Zorina, L.; Simonov, S.; Batail, P.; Brown, S.; Garcia-Garibay, M. A. *J. Am. Chem. Soc.* **2011**, *133*, 6371. (e) Rodríguez-Molina, B.; Farfán, N.; Romero, M.; Méndez-Stivalet, J. M.; Santillan, R.; Garcia-Garibay, M. A. *J. Am. Chem. Soc.* **2011**, *133*, 7280. (f) Vogelsberg, C. S.; Garcia-Garibay, M. A. *Chem. Soc. Rev.* **2012**, *41*, 1892.
- (5) (a) Katrusiak, A.; Szafranski, M. *Phys. Rev. Lett.* **1999**, *82*, 576. (b) Katrusiak, A.; Szafranski, M.; McIntyre, G. J. *Phys. Rev. Lett.* **2002**, *89*, 215507.
- (6) (a) Ye, H.-Y.; Fu, D.-W.; Zhang, Y.; Zhang, W.; Xiong, R.-G.; Huang, S. D. *J. Am. Chem. Soc.* **2009**, *131*, 42. (b) Zhang, W.; Chen, L.-Z.; Xiong, R.-G.; Nakamura, T.; Huang, S. D. *J. Am. Chem. Soc.* **2009**, *131*, 12544. (c) Zhang, W.; Ye, H.-Y.; Cai, H.-L.; Ge, J.-Z.; Xiong, R.-G.; Huang, S. D. *J. Am. Chem. Soc.* **2010**, *132*, 7300.
- (7) (a) Cai, H.-L.; Zhang, W.; Ge, J.-Z.; Zhang, Y.; Awaga, K.; Nakamura, T.; Xiong, R.-G. *Phys. Rev. Lett.* **2011**, *107*, 147601. (b) Fu, D.-W.; Zhang, W.; Cai, H.-L.; Zhang, Y.; Ge, J.-Z.; Xiong, R.-G.; Huang, S. D. *J. Am. Chem. Soc.* **2011**, *133*, 12780. (c) Xu, G.-C.; Zhang, W.; Ma, X.-M.; Chen, Y.-H.; Zhang, L.; Cai, H.-L.; Wang, Z.-M.; Xiong, R.-G.; Gao, S. *J. Am. Chem. Soc.* **2011**, *133*, 14948. (d) Zhang, W.; Cai, Y.; Xiong, R.-G.; Yoshikawa, H.; Awaga, K. *Angew. Chem., Int. Ed.* **2010**, *49*, 6608. (e) Zhang, W.; Ye, H.-Y.; Xiong, R.-G. *Coord. Chem. Rev.* **2009**, *253*, 2980. (f) Fu, D.-W.; Zhang, W.; Cai, H.-L.; Zhang, Y.; Ge, J.-Z.; Xiong, R.-G.; Huang, S. D.; Takayoshi, N. *Angew. Chem., Int. Ed.* **2011**, *50*, 11947. (g) Fu, D.-W.; Zhang, W.; Cai, H.-L.; Ge, J.-Z.; Zhang, Y.; Xiong, R.-G. *Adv. Mater.* **2011**, *23*, 5658.
- (8) (a) Akutagawa, T.; Takeda, S.; Hasegawa, T.; Nakamura, T. *J. Am. Chem. Soc.* **2004**, *126*, 291. (b) Ren, X. M.; Nishihara, S.; Akutagawa, T.; Nakamura, T. *Inorg. Chem.* **2006**, *45*, 2229.
- (9) For a convenient structural comparison of **1** in the HTP and LTP, the nonstandard setting of the room-temperature space group $Pnam$ ($a = 15.729(3)$ Å, $b = 7.795(2)$ Å, $c = 9.041(2)$ Å) is chosen to take a consistent coordinate system with the low-temperature space group $Pna2_1$ ($a = 15.830(8)$ Å, $b = 7.718(4)$ Å, $c = 9.003(4)$ Å).